Nonlinear Difference Imaging Approach to Three-Dimensional Electrical Impedance Tomography in the Presence of Geometric Modeling Errors

Dong Liu*, Ville Kolehmainen, Samuli Siltanen, Anne-Maria Laukkanen, and Aku Seppänen

Abstract—**Objective: To evaluate the recently proposed nonlinear difference imaging approach to electrical impedance tomography (EIT) in realistic 3-D geometries. Methods: In this paper, the feasibility of nonlinear difference approach-based EIT is tested using simulation studies in 3-D geometries of thorax and larynx, and with an experimental study of a thorax-shaped water tank. All test cases exhibit severe modeling errors due to uncertainty in the boundary shape of the body. Results: In all test cases, the conductivity change reconstructed with nonlinear difference imaging outperforms the conventional reconstructions qualitatively and quantitatively. Conclusion: The results demonstrate that the nonlinear difference reconstructions tolerate geometrical modeling errors at least to the same extent as the conventional linear approach and produce quantitatively more accurate information on the conductivity change. Significance: Physiological processes that produce changes in the electrical conductivity of the body can be monitored with difference imaging based on EIT. The wide popularity of linearized difference imaging in EIT is mainly based on its good tolerance for the ubiquitous modeling errors, which are predominantly caused by inexact knowledge of the body geometry. However, the linearized difference imaging produces only qualitative information on the conductivity change, and the feasibility of the estimates also depends on the selection of the linearization point which ideally should be equal to the conductivity of the initial state. Based on the findings of this paper, these problems can be avoided by nonlinear difference imaging, and potentially the approach can enable quantitative imaging of conductivity change in medical applications.**

Index Terms—**Difference imaging, electrical impedance tomography (EIT), inverse problems, modeling errors.**

Manuscript received September 22, 2015; revised November 30, 2015; accepted December 12, 2015. Date of publication December 17, 2015; date of current version August 18, 2016. This work was supported by the Academy of Finland under Project 119270, Project 134868, Project 140280, Project 250215, Project 270174, and Project 273536, Finnish Doctoral Programme in Computational Sciences, and the Finnish Center of Excellence of Inverse Problems Research 2012–2017. *Asterisk indicates corresponding author.*

*D. Liu is with the Department of Applied Physics, University of Eastern Finland, Kuopio 70211, Finland (e-mail: dong.liu@outlook.com).

V. Kolehmainen and A. Seppänen are with the Department of Applied Physics, University of Eastern Finland.

S. Siltanen is with the Department of Mathematics and Statistics, University of Helsinki.

A. M. Laukkanen is with the Speech and Voice Research Laboratory, University of Tampere.

Color versions of one or more of the figures in this paper are available online at http://ieeexplore.ieee.org.

Digital Object Identifier 10.1109/TBME.2015.2509508

I. Introduction

ELECTRICAL impedance tomography (EIT) is an imaging technology in which the electrical conductivity of a body is estimated as a spatially distributed parameter based on measurements of electrical currents and potentials at the boundary of the body. The feasibility studies on potential clinical applications of EIT have focused on applications such as monitoring lung [1], [2] and heart functions and detecting breast cancer [3]–[5].

Methods of EIT imaging can be divided to *absolute imaging* [4], [6] and *difference imaging* [7]–[10].

In absolute imaging, the conductivity distribution is estimated using a single set of potential measurements, during which the conductivity is modeled invariant. The realization of absolute imaging for medical applications has been largely hampered by the ill-posedness of the EIT problem; the image reconstruction is very sensitive to the ubiquitous modeling errors which are caused by inaccurately known auxiliary variables of the measurement model. In particular, the shape of the body is in practice always inaccurately known, and it has been shown that especially the errors in modeling of the body shape produce severe errors in the absolute reconstructions [11], [12].

In difference imaging, a change in the conductivity is estimated based on datasets measured before and after the conductivity change. Conventionally, the reconstruction of the conductivity change is carried out using a *linear approach* where one approximates the nonlinear observation model by a linearized model and by taking difference of the data before and after the change. In this approach, the reconstruction of the conductivity change becomes a linear problem which can be solved, for example, by regularized linear least squares (LS) approach. The main benefit and reason for the popularity of the linear approach is its good tolerance to modeling errors caused by the inaccurately known auxiliary model parameters. This feature stems from partial cancellation of (invariant) modeling errors in the subtraction of the data before the change from the data after the change.

Although the linear approach to difference imaging is able to suppress some of the effects of geometrical modeling errors, it has been shown that artifacts are still present in the reconstructions [13]–[15]. Furthermore, a drawback of the linear approach is that the linear approximation for the nonlinear forward model is only feasible for small deviations from the

linearization point [16]. In high contrast cases, such as accumulation of well conducting liquid (haematothorax) or poorly conducting air (pneumothorax) in the lungs, the linear approach may prevent the detection of clinically relevant changes [17]. The performance of the linear approach also depends on the selection of the linearization point, which should ideally be equal to the unknown initial state. Conventionally, the linearization point is selected as a homogeneous estimate of the conductivity of the initial state. However, in practical medical applications, the initial state is often highly inhomogeneous. Therefore, difference imaging with linear approach provides only qualitative information on the conductivity change.

Apart from the linear approach to difference imaging, another approach to use two measurement sets for estimating the conductivity change is to carry out the absolute reconstructions of conductivities σ_1 and σ_2 based on each of the datasets separately, and to subtract σ_1 from σ_2. The change estimate $\widehat{\delta\sigma}$ is often relatively feasible because the artifacts due to the modeling errors are similar in the estimated conductivities $\hat{\sigma}_1$ and $\hat{\sigma}_2$, and are partly canceled in the subtraction $\hat{\sigma}_2 - \hat{\sigma}_1$; for an example, see [18].

In [19], a nonlinear approach to difference imaging was proposed. The approach is based on regularized nonlinear LS framework. The EIT measurements before and after the change are concatenated into a single measurement vector, and both the initial conductivity and the conductivity change are simultaneously reconstructed based on the combined data. A key feature of this approach is that the conductivity after the change is parameterized as a linear combination of the initial state and the conductivity change. Therefore, it naturally allows for modeling independently the spatial characteristics of the initial conductivity (background) and the conductivity change by using different regularization functionals. The approach also allows us to restrict the conductivity change to a subvolume in a straightforward way when the conductivity change is known to occur in some specific region of interest (ROI) inside the body.

In [20], the tolerance of the nonlinear approach for the modeling errors was studied with 2-D simulations. The quality of the reconstructions with the nonlinear approach was found to be superior compared to the conventional linear difference and absolute reconstructions in the presence of modeling errors resulting from domain truncation, unknown contact impedances, inaccurately known electrode locations, and inaccurately known domain boundary.

In this paper, we study the feasibility of the nonlinear difference reconstruction approach in 3-D difference imaging. The special focus is in studying the robustness of the approach with respect to geometrical modeling errors in realistic 3-D geometries related to three potential medical applications of EIT: monitoring of vocal folds in voice loading studies [19], [21], cardiac imaging [22], [23], and lung imaging [1], [2]. In the simulation studies of this paper, computerized tomography (CT) images are used for modeling the geometries of the neck and thorax for the simulation of the EIT measurement data. The approach is also tested using experimental EIT data from a thorax-shaped water tank. In the image reconstruction, approximative geometrical models are used to simulate practical situations where the accurate shape of the body is not available. The results are compared against the conventional linear and absolute reconstructions.

The rest of this paper is organized as follows. In Section II, a brief review of the EIT forward model is given. The properties of the absolute and difference imaging are outlined in Section III. In Section IV, the target and model domains and simulation of measurements and test cases are explained. Results and discussion are given in Section V, and conclusion is drawn in Section VI.

II. EIT Forward Model

Let $\Omega \subset \mathbb{R}^3$ denote the target domain. In EIT, L contact electrodes are attached to the positions $e_\ell \subset \partial\Omega$ $\ell = 1, 2, \ldots, L$ on the boundary $\partial\Omega$. A set of electric currents is injected into the body through these electrodes, and the resulting voltages are measured using the same electrodes. For modeling these measurements, we utilize the so-called complete electrode model [24], which consists of the following partial differential equation and the boundary conditions:

$$\nabla \cdot (\sigma(x)\nabla u(x)) = 0, \quad x \in \Omega \tag{1}$$

$$u(x) + z_\ell \sigma(x) \frac{\partial u(x)}{\partial n} = U_\ell, \quad x \in e_\ell,\ \ell = 1, \ldots, L \tag{2}$$

$$\int_{e_\ell} \sigma(x) \frac{\partial u(x)}{\partial n}\, \mathrm{d}S = I_\ell, \quad \ell = 1, \ldots, L \tag{3}$$

$$\sigma(x) \frac{\partial u(x)}{\partial n} = 0, \quad x \in \partial\Omega \backslash \bigcup_{\ell=1}^{L} e_\ell \tag{4}$$

where $\sigma(x)$ is the conductivity, $u(x)$ is the electric potential distribution inside the target domain Ω, $x \in \Omega$ is the spatial coordinate, and n denotes the outward unit normal vector on the boundary $\partial\Omega$. Contact impedances, electrode potentials, and injected currents corresponding to the electrodes e_ℓ, $\ell = 1, \ldots, L$ are denoted by z_ℓ, U_ℓ, and I_ℓ, respectively. The currents satisfy the charge conservation law

$$\sum_{\ell=1}^{L} I_\ell = 0 \tag{5}$$

and a ground level for the potentials can be fixed by

$$\sum_{\ell=1}^{L} U_\ell = 0. \tag{6}$$

The numerical solution of the model (1)–(6) is often based on the finite element method (FEM) [6]. In the finite element (FE) scheme, we write approximations

$$\sigma(x) = \sum_{k=1}^{N_\sigma} \sigma_k \phi_k(x) \tag{7}$$

$$u(x) = \sum_{j=1}^{N_u} \alpha_j \psi_j(x) \tag{8}$$

for the functions $\sigma(x)$ and $u(x)$ in the variational form [25] of (1)–(6). Here, N_σ and N_u are the numbers of nodes in the FE meshes that are used for the representations of $\sigma(x)$ and $u(x)$. Further, $\phi_k(x)$ and $\psi_j(x)$ are the nodal basis functions that are used for the conductivity and the potential, respectively. Then, using a standard Galerkin discretization, the solution of the forward problem becomes equivalent to solving a system of linear equations. In the following, we denote the discretized forward mapping $\sigma \mapsto U(\sigma)$ by $U(\sigma)$. For details of the FE approximation, see [6] and [25].

Using an additive Gaussian model for the measurement errors, the observation model becomes

$$V = U(\sigma) + e \tag{9}$$

where $V \in \mathbb{R}^M$ is the vector including all the measured electrode potentials $M = mN_{\text{inj}}$, where N_{inj} denotes the number of current injections, and m is the number of measured potentials for each current injection. Moreover, $e \in \mathbb{R}^M$ is the Gaussian distributed measurement noise $e \sim \mathcal{N}(e^*, \Gamma_e)$. The mean $e^* \in \mathbb{R}^M$ and the covariance matrix $\Gamma_e \in \mathbb{R}^{M\times M}$ are usually estimated experimentally, see [26].

III. Image Reconstruction

A. Absolute Imaging

In absolute imaging, the (static) conductivity σ is reconstructed by using a single set of measurements V. The most popular reconstruction method for absolute imaging is the *generalized Tikhonov regularization*

$$\hat{\sigma} = \arg\min_{\sigma>0}\{\|L_e(V - U(\sigma))\|^2 + p_\sigma(\sigma)\} \tag{10}$$

where L_e is a Cholesky factor of the noise precision matrix, i.e., $L_e^{\mathrm{T}} L_e = \Gamma_e^{-1}$, and $p_\sigma(\sigma)$ is the regularization functional that stabilizes the inversion.

B. Difference Imaging

Difference imaging aims at estimating the conductivity change $\delta\sigma$ between two EIT measurements V_1 and V_2 at time instants t_1 and t_2, respectively. The observation models corresponding to the two EIT measurements can be written as

$$V_1 = U(\sigma_1) + e_1 \tag{11}$$

$$V_2 = U(\sigma_2) + e_2 \tag{12}$$

where $e_i \sim \mathcal{N}(e_i^*, \Gamma_{e_i})$, $i = 1, 2$. Notice that typically the noise is modeled stationary in the sense that $e_i^* = e^*, i = 1, 2$ and $\Gamma_{e_i} = \Gamma_e, i = 1, 2$. This model is also employed in this paper.

1) Linear Approach: In the conventional linear approach to difference imaging, models (11) and (12) are approximated by first-order Taylor approximations as

$$V_i \approx U(\sigma_0) + J(\sigma_i - \sigma_0) + e_i, \quad i = 1, 2 \tag{13}$$

where σ_0 is the linearization point, and $J = \frac{\partial U}{\partial \sigma}(\sigma_0)$ is the Jacobian matrix evaluated at σ_0. Using the linearizations and subtracting V_1 from V_2 gives the observation model

$$\delta V \approx J\delta\sigma + \delta e \tag{14}$$

where $\delta V = V_2 - V_1$, $\delta\sigma = \sigma_2 - \sigma_1$, and $\delta e = e_2 - e_1$.

A Tikhonov regularized solution based on the linearized observation model (14) is of the form

$$\widehat{\delta\sigma} = \arg\min_{\delta\sigma}\{\|L_{\delta e}(\delta V - J\delta\sigma)\|^2 + p_{\delta\sigma}(\delta\sigma)\}. \tag{15}$$

Here, the weighting matrix $L_{\delta e}$ is defined as $L_{\delta e}^{\mathrm{T}} L_{\delta e} = \Gamma_{\delta e}^{-1}$, where $\Gamma_{\delta e}$, the covariance of the noise term δe, is $\Gamma_{\delta e} = \Gamma_{e_1} + \Gamma_{e_2} = 2\Gamma_e$.

2) Nonlinear Approach: The nonlinear approach to difference imaging, proposed in [19], aims at simultaneous reconstruction of the initial σ_1 and the change $\delta\sigma$ based on measurements V_1 and V_2. The key idea in the approach is that the conductivity σ_2 is modeled as a linear combination of the initial state σ_1 and the change $\delta\sigma$. One feature of this parameterization is that it offers a straightforward way to restrict the conductivity change $\delta\sigma$ to a ROI, if temporal changes are known to occur only in a subvolume inside the body. Let

$$\operatorname{supp}(\delta\sigma) = \Omega_{\text{ROI}} \subseteq \Omega$$

denote the ROI and denote the conductivity change within Ω_{ROI} by $\delta\sigma_{\text{ROI}}$. Obviously, case $\Omega_{\text{ROI}} = \Omega$ corresponds to the case where there is no ROI constraint on the conductivity change. Then, we write

$$\delta\sigma = \mathcal{K}\delta\sigma_{\text{ROI}}$$

where $\mathcal{K}$ is an extension mapping $\mathcal{K} : \Omega_{\text{ROI}} \to \Omega$ such that

$$\mathcal{K}\delta\sigma_{\text{ROI}} = \begin{cases} \delta\sigma_{\text{ROI}}, & x \in \Omega_{\text{ROI}} \\ 0, & x \in \Omega \setminus \Omega_{\text{ROI}} \end{cases} \tag{16}$$

and the conductivity σ_2 after the change is modeled as

$$\sigma_2 = \sigma_1 + \mathcal{K}\delta\sigma_{\text{ROI}}. \tag{17}$$

Inserting model (17) into (12) and concatenating the measurement vectors V_1 and V_2 and the corresponding models in (11) and (12) into block vectors leads to the observation model

$$\underbrace{\begin{bmatrix} V_1 \\ V_2 \end{bmatrix}}_{\bar{V}} = \underbrace{\begin{bmatrix} U(\sigma_1) \\ U(\sigma_1 + \mathcal{K}\delta\sigma_{\text{ROI}}) \end{bmatrix}}_{\bar{U}(\bar{\sigma})} + \underbrace{\begin{bmatrix} e_1 \\ e_2 \end{bmatrix}}_{\bar{e}} \tag{18}$$

or

$$\bar{V} = \bar{U}(\bar{\sigma}) + \bar{e} \tag{19}$$

where

$$\bar{\sigma} = \begin{bmatrix} \sigma_1 \\ \delta\sigma_{\text{ROI}} \end{bmatrix}.$$

The estimate of $\bar{\sigma}$ is obtained as

$$\hat{\bar{\sigma}} = \arg\min_{\bar{\sigma}}\{\|L_{\bar{e}}(\bar{V} - \bar{U}(\bar{\sigma}))\|^2 + p_{\bar{\sigma}}(\bar{\sigma})\} \tag{20}$$

$$\text{s.t. } \sigma_1 > 0,\ \sigma_1 + \mathcal{K}\delta\sigma_{\text{ROI}} > 0$$

where $L_{\bar{e}} \in \mathbb{R}^{2M\times 2M}$ such that $L_{\bar{e}}^{\mathrm{T}} L_{\bar{e}} = \Gamma_{\bar{e}}^{-1}$ and

$$\Gamma_{\bar{e}} = \begin{bmatrix} \Gamma_{e_1} & \mathbf{0}_{M\times M} \\ \mathbf{0}_{M\times M} & \Gamma_{e_2} \end{bmatrix}.$$

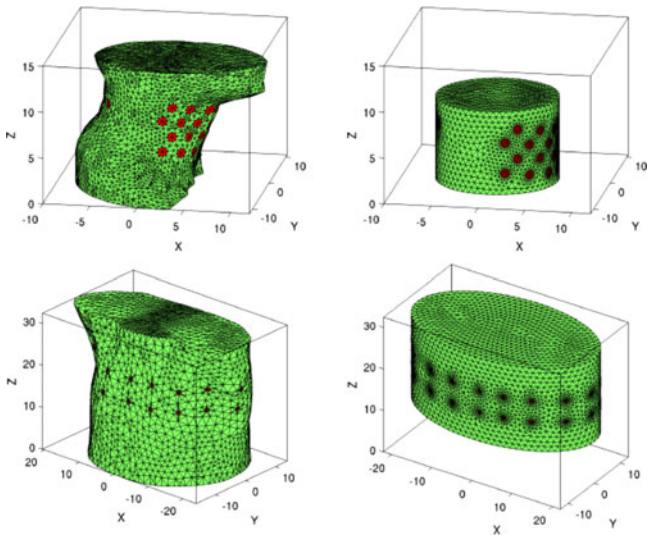

Fig. 1. Meshes used for numerical studies. Left: meshes of the human neck domain and thorax domain for simulating measurements. Right: meshes of the model domains for the inverse computations.

TABLE I
3-D FE MESHES FOR THE TEST CASES

	Simulated data		Reconstruction		
	N_u	N_σ	N_u	N_σ	N_{ROI}
Case 1	95 620	13 270	70 602	8700	2653
Case 2	196 171	25 528	64 128	9255	936
Cases 3 and 4	196 171	25 528	64 128	9255	9255
	Experimental data		Reconstruction		
			N_u	N_σ	N_{ROI}
Case 5			48 285	6929	539
Case 6			48 285	6929	785

N_u is the number of nodes in the second-order polynomial FE mesh for approximation of u_x, and N_σ is the number of node points in the first-order polynomial FE mesh for approximation of $\sigma(x)$. N_{ROI} is the number of conductivity nodes in the ROI. Columns 2 and 3 show the numbers of nodes and elements in the meshes used for simulating measurements. Columns 4 and 6 show the numbers of nodes and elements in the meshes for computing the reconstructions (E1)–(E5).

In this paper, the noise statistics are modeled stationary, i.e., $\Gamma_{e_1} = \Gamma_{e_2} = \Gamma_e$. The regularization functional $p_{\bar{\sigma}}(\bar{\sigma})$ is defined as

$$p_{\bar{\sigma}}(\bar{\sigma}) = p_{\sigma_1}(\sigma_1) + p_{\delta\sigma_{\mathrm{ROI}}}(\delta\sigma_{\mathrm{ROI}})$$

which naturally allows designing different spatial models for σ_1 and $\delta\sigma$ in cases where the spatial characteristics of the initial state σ_1 and the change $\delta\sigma$ are different. For example, if one would expect a sharp piecewise regular change $\delta\sigma$ and a smooth initial conductivity σ_1, $p_{\sigma_1}(\sigma_1)$ could be chosen as smoothness regularization and $p_{\delta\sigma_{\mathrm{ROI}}}(\delta\sigma_{\mathrm{ROI}})$ as total variation (TV) regularization.

In [20], it was demonstrated that the nonlinear difference reconstructions tolerate well a variety of modeling errors in 2-D. In the presence of errors induced by truncation of the model domain, inaccurately known electrode positions and boundary shape, as well as unknown contact impedance values, the nonlinear difference imaging was shown to produce better estimates of the conductivity change than the conventional approaches.

IV. METHODS

In this section, we describe the models used in the simulation studies, the computed estimates, and the experimental setup. In the simulation studies, the 3-D geometries correspond to applications of EIT to glottal, cardiac, and lung imaging. In the experimental studies, a water tank with human thorax shape is used.

A. Target and Model Domains

The left column in Fig. 1 shows the FE meshes of the neck and chest that were used for the simulation of the measurement data. The geometries of the neck and thorax were obtained from CT images.

In the neck model, $L = 32$ disc electrodes with a radius of 0.5 cm were modeled on the boundary $\partial\Omega$. Electrodes 1 through 28 in a 7×4 array were placed on the frontal part of the domain boundary near the glottal area, whereas the other 4 electrodes were horizontally placed on the back side of the domain boundary. In the thorax model, $L = 32$ disc electrodes with a radius of 0.5 cm were arranged in two horizontal rows of 16 approximately equally spaced electrodes. The locations of electrodes are indicated by red color in Fig. 1.

To study the effect of modeling errors caused by inaccurately known shape of the target domain, we used approximate model domains in the image reconstruction problem. The right column in Fig. 1 shows the model domains for the neck and chest. For the neck geometry, the model domain was a cylinder with radius 6.5 cm and height 9 cm. For the chest, an elliptic cylinder with height 20 cm, semimajor axis 22 cm, and semiminor axis 13 cm was used as the model domain. Note that both model domains were also truncated in the z-direction. The discretization details of the target domain and model domain in each test case are given in Table I.

To further illustrate the geometrical modeling errors, sets of horizontal cross sections of the target and model domains are shown in Fig. 2. The volume of the target domain was 1.9 L for the human neck and 25.5 L for the thorax, while the volumes of the respective model domains used in the inverse computations were 1.2 and 18.0 L.

B. Simulation of EIT Measurements

In the simulation of the EIT measurements, 32 "Skip-3" (for details, see [27, p. 176]) current patterns were used and the voltages were measured between adjacent electrode pairs, leading to 1024 voltage measurements, that is, $V \in \mathbb{R}^{1024}$. The amplitude of the current was 1 mA, and the contact impedances z_ℓ were set to $100\,\Omega \cdot \mathrm{cm}^2$ for all the electrodes. The conductivities of the tissues used in the simulations are shown in Table II. The EIT data were computed using the FEM.

To simulate the measurement noise, Gaussian random noise with standard deviation 0.05% of the difference between the

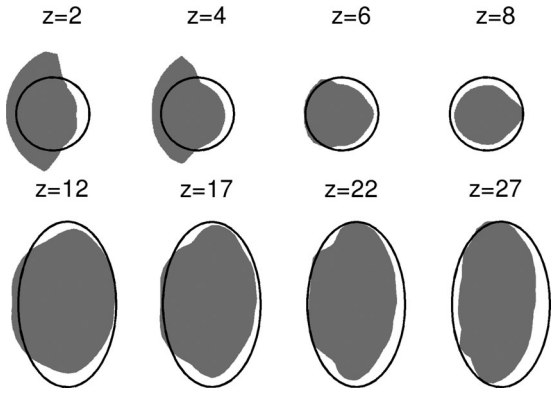

Fig. 2. Horizontal cross sections of the target domains, and the boundaries of the model domains $\hat{\Omega}$ ($\partial\hat{\Omega}$ is shown with solid line) at different heights. Top: human neck domain. Bottom: thorax domain.

TABLE II
CONDUCTIVITY VALUES USED IN THE SIMULATION [28]

Tissue	Conductivity (mS/cm)
Vocal folds	3.6
Soft tissue	2.0
Deflated lung	1.5
Inflated lung	0.5
Collapsed lung	1.0
Cardiac muscle	1.5
Blood	5.5
Heart (mixture of blood and heart)	3.5

maximum and minimum value of the noiseless voltages was added to the measurements V_1 and V_2 in each test case. We note that with this noise model, the variances of the simulated noise in measurements V_2 are not equal to those in V_1. When solving the inverse problem, however, the noise statistics was modeled stationary, as noted in Section III-B2.

C. Estimates

The following estimates were computed.

E1) *Absolute reconstructions* of σ_1 and σ_2 by solving

$$\hat{\sigma}_i = \arg\min_{\sigma_i>0}\{\|L_e(V_i - U(\sigma_i))\|^2 + \|L_\sigma(\sigma_i - \sigma^*)\|^2\}$$

where σ^* is the expectation of σ_i and $L_\sigma^{\mathrm{T}} L_\sigma = \Gamma_\sigma^{-1}$, and Γ_σ is a smoothness promoting covariance matrix with elements defined as

$$\Gamma_\sigma(j,k) = a\exp\left\{-\frac{\|x_j - x_k\|_2^2}{2b^2}\right\} + c\delta_{jk}. \quad (21)$$

Here, $\Gamma_\sigma(j,k)$ is the covariance matrix element (j,k) corresponding to the conductivities at the nodes in locations x_j and x_k; a, b, and c are positive scalar parameters, and δ_{jk} denotes the Kronecker delta function. Parameter a can be used to tune the variation (contrast) of the conductivity, parameter b sets the correlation length (smoothness) of the model, and c is a small positive parameter which is used to guarantee that inverse of Γ_σ exists. For further details, see [29].

From these reconstructions, the estimate for the conductivity change was simply obtained by $\widehat{\delta\sigma} = \hat{\sigma}_2 - \hat{\sigma}_1$ [18].

E2) Conventional *linear difference reconstruction* of $\delta\sigma$ by solving

$$\widehat{\delta\sigma} = \arg\min_{\delta\sigma}\{\|L_{\delta e}(\delta V - J\delta\sigma)\|^2 + \|L_{\delta\sigma}\delta\sigma\|^2\} \quad (22)$$

where $L_{\delta\sigma}^{\mathrm{T}} L_{\delta\sigma} = \Gamma_{\delta\sigma}^{-1}$ and $\Gamma_{\delta\sigma}$ was constructed by (21).

E3) *ROI constrained linear difference reconstruction* of $\delta\sigma_{\mathrm{ROI}}$ in the subvolume Ω_{ROI} by solving

$$\widehat{\delta\sigma}_{\Omega_{\mathrm{ROI}}} = \arg\min_{\delta\sigma_{\Omega_{\mathrm{ROI}}}} \{\|L_{\delta e}(\delta V - J_{\Omega_{\mathrm{ROI}}}\delta\sigma_{\Omega_{\mathrm{ROI}}})\|^2 + \|L_{\delta\sigma_{\Omega_{\mathrm{ROI}}}}\delta\sigma_{\Omega_{\mathrm{ROI}}}\|^2\}.$$

Here, $J_{\Omega_{\mathrm{ROI}}} = J\mathcal{K}$, $L_{\delta\sigma_{\Omega_{\mathrm{ROI}}}}^{\mathrm{T}} L_{\delta\sigma_{\Omega_{\mathrm{ROI}}}} = \Gamma_{\delta\sigma_{\Omega_{\mathrm{ROI}}}}^{-1}$ and $\Gamma_{\delta\sigma_{\Omega_{\mathrm{ROI}}}} = \mathcal{K}^{\mathrm{T}}\Gamma_{\delta\sigma}\mathcal{K}$.

This estimate was computed as a reference of how the linear approach performs when a ROI constraint is employed.

E4) Estimate of $\bar{\sigma} = (\sigma_1^{\mathrm{T}}, \delta\sigma_{\mathrm{ROI}}^{\mathrm{T}})^{\mathrm{T}}$ with the *nonlinear difference reconstruction*

$$\hat{\bar{\sigma}} = \arg\min_{\bar{\sigma}}\left\{\|L_{\bar{e}}(\bar{V} - \bar{U}(\bar{\sigma}))\|^2 + p_{\bar{\sigma}}(\bar{\sigma})\right\}$$
$$\text{s.t. } \sigma_1 > 0,\ \sigma_1 + \mathcal{K}\delta\sigma_{\mathrm{ROI}} > 0$$

with the choice

$$p_{\bar{\sigma}}(\bar{\sigma}) = \|L_{\sigma_1}(\sigma_1 - \sigma^*)\|^2 + \alpha\mathrm{TV}(\delta\sigma_{\mathrm{ROI}})$$

where $\alpha > 0$ is a weighting parameter, and

$$\mathrm{TV}(\sigma) = \sum_{k=1}^{N_e} |e_k|\sqrt{\|(\nabla\sigma)|_{e_k}\|^2 + \beta} \quad (23)$$

is a differentiable approximation of the isotropic TV functional [30], $(\nabla\sigma)|_{e_k}$ is the (constant) gradient of the (piecewise linear) σ at element e_k, and N_e is the number of elements in the mesh that is used for the conductivity, $\beta > 0$ is a small parameter which ensures that $\mathrm{TV}(\sigma)$ is differentiable. In all test cases, the subdomain Ω_{ROI} in the estimates (E3) and (E4) was the same.

E5) Estimate of $\bar{\sigma} = (\sigma_1^{\mathrm{T}}, \delta\sigma^{\mathrm{T}})^{\mathrm{T}}$ with the *nonlinear difference reconstruction* in the case where $\Omega_{\mathrm{ROI}} = \Omega$. That is, estimate (E5) provided a nonlinear difference reconstruction in a case where no ROI constraints were used. Here, $p_{\bar{\sigma}}(\bar{\sigma})$ was chosen as in (E4) (with $\Omega_{\mathrm{ROI}} = \Omega$) .

The minimization problems in (E1), (E4), and (E5) were solved by using the Gauss–Newton method with a line search.

D. Prior Parameters

The parameters a, b, c of the covariance (21) and α, β of the TV functional (22) were selected based on simulations. The values are listed for each of the test cases in Table III. For the Bayesian interpretation of the parameters of the model (21), see

TABLE III
PRIOR PARAMETERS AND ROI INFORMATION

	Simulated data				Experimental data	
	Case 1	Case 2	Case 3	Case 4	Case 5	Case 6
a	2.5	1.0	1.0	1.0	1.5×10^{-2}	1.5×10^{-2}
b	1	1.5	1.5	1.5	2	2
c	0.001	0.001	0.001	0.001	1.5×10^{-5}	1.5×10^{-5}
α	0.04	0.04	0.04	0.04	1.5	1.5
β	0.001	0.001	0.001	0.001	1×10^{-4}	1×10^{-4}
h_1	1	15			9.5	9.5
h_2	6	25	$\Omega_{\mathrm{ROI}} = \Omega$		25.5	25.5
r_0	3	10			10	10
(x_0, y_0)	(3.25, 0)	(2.5, 2.5)			(−8.5, −3.5)	(−3.5, −5.5)

[31], [32]. For a Bayesian interpretation of the TV model (22) and for a systematic approach to select the parameter α based on the expected magnitude of the changes in σ, see [33].

In the estimates (E1), (E4), and (E5), the expectation $\sigma^* \in \mathbb{R}$ for the conductivity was computed by solving the best homogeneous conductivity estimate using the data V_1 from the initial state

$$\sigma^* = \arg\min_{\sigma>0} \|L_e(V_1 - U(\sigma))\|^2.$$

Note that measurements with homogeneous background were not used in any of the following cases.

In each test case, the ROI in estimates (E3) and (E4) was a cylinder

$$\Omega_{\mathrm{ROI}} = D_{\mathrm{ROI}} \times (h_1, h_2) \subset \mathbb{R}^3$$

where $D_{\mathrm{ROI}} \subset \mathbb{R}^2$ is a disk with center point at (x_0, y_0) and radius r_0. The location and size parameters r_0, x_0, y_0, h_1, and h_2 of the ROIs can be found in Table III.

E. Simulation Examples

To study the performance of the nonlinear approach in realistic 3-D geometries, the following four simulation cases were carried out. In each test case, two measurement sets were simulated: V_1 corresponding to an initial conductivity σ_1 and V_2 corresponding to conductivity σ_2 after the change.

1) *Case 1: Glottal imaging with EIT*. In this test case, the initial state σ_1 simulates a case where the glottis is closed by holding breath, and the conductivity after the change σ_2 corresponds to a case where the glottis is partially open, forming a nonconductive strip within the glottis.
2) *Case 2: Cardiac imaging with EIT*. The initial state σ_1 simulates a heart in the end-systolic phase, and the conductivity after the change σ_2 simulates the heart in the end-diastolic phase. Notice that the model is ideal in the sense that there is no change of shape of the thorax and the conductivity of the lungs. However, in a practical situation, one could avoid significant changes of the subject's thorax shape and the conductivity of the lungs by asking the subjects to inspire and then hold their breath for a short measurement time.

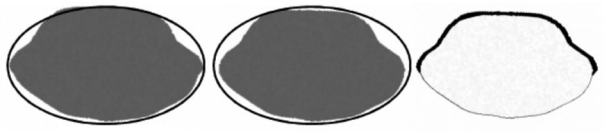

Fig. 3. Study of the lung imaging with a shape change of the thorax in Case 4. Horizontal cross section of the model domain $\hat{\Omega}$ ($\partial\hat{\Omega}$ is shown with solid line) and the target domain Ω (shown as gray patch). Left: thorax at the end-inspiration phase. Middle: thorax at the end-expiration phase. Right: the change of the thorax shape (shown as black patch). When the thorax is in the end-expiration phase, the volume of the thoracic cavity and the size of a lung decrease by 4.15% and 15%, respectively.

3) *Case 3: Lung imaging without a change of the thorax shape*. In the simulation, the initial state σ_1 corresponds to the end-inspiration phase, and the conductivity after the change σ_2 corresponds to the end-expiration phase. This test case was done to produce a reference case of lung imaging, where the geometric modeling errors between the initial state and the state after the change are invariant in the sense that the geometry is the same in both V_1 and V_2.
4) *Case 4: Lung imaging with a change of the thorax shape.* In clinical situations, the thorax shape varies due to breathing and changes of the patient position during the measurements. For this reason, we simulate a more realistic case in lung monitoring, where the shape changes due to breathing, leading to a situation where all the estimates (E1–E5) are more prone to the modeling errors since the (unknown) body geometry in V_1 and V_2 is not the same. The change of the thorax shape is simulated by linear movement and deformation of the front part of the chest, leading to 4.15% change in the volume of the thoracic cavity and 15% change in the lung volume between the initial state and the state after the change, see Fig. 3.

Again, we note that Case 3 where chest shape does not change between states σ_1 and σ_2 is not a realistic one. The reason for considering both Case 3 and Case 4 is to study separately the effects of modeling errors that are equal between the two states and the errors that vary between the states.

In Case 4, the 4.15% volume change of thoracic cavity is simulated by lengthening the chest dimension in the anterior–posterior direction by 5%. We assume this to correspond to a case of normal/light breathing—according to the literature [11], [34], the maximal extension of the chest dimension in the anterior–posterior direction is 10%. Moreover, the simulations model cases where 3/4 of the lung volume is collapsed, and in the inspiration the lung size is increased by 15%, which is about 1/4 of a typical volume change in a healthy lung [35].

F. Experimental Setup and Test Cases

The experimental data (Cases 5 and 6) was measured from a human thorax-shaped water tank, see Fig. 4. $L = 48$ disc electrodes with a radius of 1.5 cm were arranged in three horizontal arrays; 16 approximately equally spaced electrodes per array. The outer circumferences of the top, middle, and bottom layers of electrodes were 107, 111, and 115 cm, respectively. The

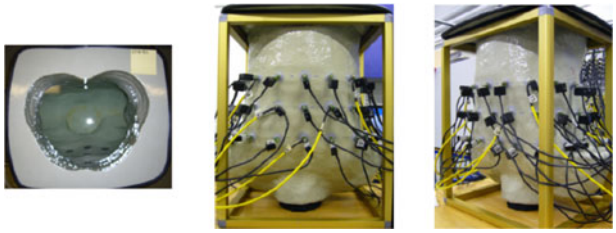

Fig. 4. Measurement tank. Left: the top view. Middle: the front view. Right: the side view.

space between the top and the middle layers was 5.2 cm, and the space between the middle and the bottom layers was 5.0 cm.

In both experiments, the tank was filled with tap water. In Case 5, two plastic rectangular cuboids were placed in the tank to create a nonhomogeneous background conductivity σ_1. For the state after the change σ_2, a plastic equilateral triangular prism was added to the tank, see the left column of Fig. 9. Thus, in Case 5, the contrast of the conductivity change was high. In Case 6, a low contrast conductivity change was studied. One plastic rectangular cuboid was placed in the tank to create nonhomogeneous σ_1, and for σ_2, an approximately triangular prism-shaped piece of fresh rutabaga was added to the tank. The water content of a fresh rutabaga is higher than 80%, and its conductivity is close to the background (water) conductivity.

The measurements were carried out with the KIT-4 measurement system [36]. Sixteen electrodes $\{1, 5, 9, 13, 18, 20, 22, 24, 26, 28, 30, 32, 35, 39, 43, 47\}$ were selected as the current injecting electrodes. In the EIT measurements, the frequency of the injected current was set to 10 kHz and the amplitude was 1 mA, and pairwise current injections were applied, in such a way that one electrode was fixed as the sink electrode and then applying pairwise currents sequentially between the sink electrode and each one of the 15 remaining injection electrodes.

This process was repeated using electrodes $\{1, 9, 35, 43\}$ as the sink, leading to a total of 60 current injections. Corresponding to each current injection, the potentials on all 48 electrodes were measured. With this measurement protocol, one measurement frame consists of 2880 potential readings (i.e., $V_i \in \mathbb{R}^{2880}$).

V. Results and Discussion

The true conductivity distributions and the estimates (E1)–(E5) for the simulated test cases are shown in Figs. 5–8. In each of these figures, the top three rows show the horizontal cross sections of the true conductivity distributions and the corresponding estimates, while the bottom three rows show the vertical cross sections of the true conductivity distributions and the corresponding estimates. In Figs. 5–8, the images of the conductivity changes $\delta\sigma$ are highlighted with dashed boxes because the main interest in this study lies in the reconstruction of $\delta\sigma$. In the estimates (E3) and (E4), the boundary of the ROI is indicated by a black line. In the estimates (E4) and (E5), the conductivity after the change is computed from the estimated parameters $(\hat{\sigma}_1, \widehat{\delta\sigma}_{\mathrm{ROI}})$ as

$$\hat{\sigma}_2 = \hat{\sigma}_1 + \mathcal{K}\widehat{\delta\sigma}_{\mathrm{ROI}}.$$

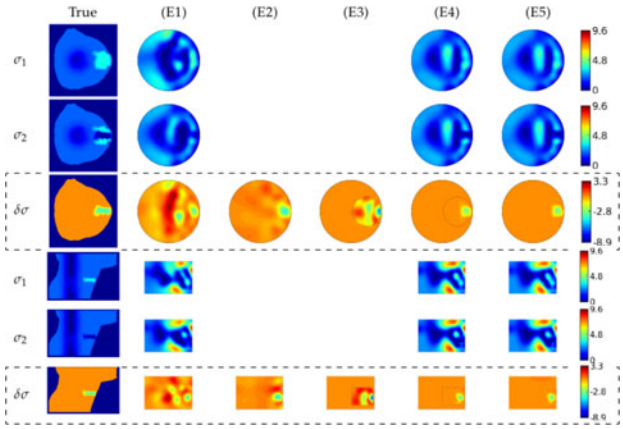

Fig. 5. Case 1: Horizontal and vertical cross sections of the neck with simulated conductivity distributions and the reconstructions obtained by estimates (E1)–(E5) described in Section IV-C. The dashed boxes highlight the true and estimated conductivity change $\delta\sigma$. (E4) and (E5) are the nonlinear difference reconstructions with and without ROI constraint, respectively.

To assess quantitatively the recovery of $\delta\sigma$ in the estimates (E1)–(E5), a relative size coverage ratio (RCR) was used to measure how well the volumes of inclusions were recovered:

$$\mathrm{RCR} = \frac{\mathrm{CR}}{\mathrm{CR}_{\mathrm{True}}}$$

where CR denotes the coverage ratio defined as the ratio of the volume of the inclusion to the total volume of the target

$$\mathrm{CR} = \frac{\text{Inclusion volume}}{\text{Target volume}} \times 100\%.$$

Correspondingly, $\mathrm{CR}_{\mathrm{True}}$ is the CR of the true target. For estimating the volume of the inclusion, we used the half value of the minimum/maximum of the estimate $\widehat{\delta\sigma}$ as the threshold for the inclusion detection [37], [38].

Further, the maximum/minimum of the reconstructed change was used to measure the accuracy of the recovered contrast. The contrasts of the reconstructed conductivity changes are tabulated in terms of a relative contrast (RCo)

$$\mathrm{RCo} = \frac{\max|\widehat{\delta\sigma}|}{\max|\delta\sigma_{\mathrm{true}}|}.$$

The relative quantities RCR and RCo are used here instead of the respective quantities CR and $\max|\widehat{\delta\sigma}|$ to ease the comparison of the values in Table IV. For both RCR and RCo, value 1 would indicate exact match of the true and estimated values of the change, while a value greater or less than 1 would indicate overestimation or underestimation, respectively.

A. Case 1: Glottal Imaging With EIT

Fig. 5 shows the results of Case 1. The reconstructions of the absolute conductivities σ_1 and σ_2 with (E1) are heavily affected by the geometric modeling errors. The subtraction $\hat{\sigma}_2 - \hat{\sigma}_1$ removes only part of the artifacts, leading to erroneous estimate of $\delta\sigma$. In the conventional linear estimate (E2), the change is recovered relatively well, and the RCR is already much closer to the true value than in (E1), see Table IV. However, (E2)

TABLE IV
RCRs AND THE RCo VALUE OF THE RECONSTRUCTED CONDUCTIVITY CHANGE $\delta\sigma$

	Simulated data								Experimental data	
	Case 1		Case 2		Case 3		Case 4		Case 5	Case 6
	RCR	RCo	RCR	RCo	RCR	RCo	RCR	RCo	RCR	RCR
(True)	1.00	1.00	1.00	1.00	1.00	1.00	1.00	1.00	1.00	1.00
(E1)	4.91	1.15	2.17	0.35	0.20	1.96	0.26	1.42	1.29	2.15
(E2)	1.77	1.31	2.30	0.20	0.39	2.59	0.41	2.06	0.96	0.49
(E3)	0.32	2.63	1.37	0.37	–	–	–	–	0.91	0.72
(E4)	0.86	1.12	0.53	1.23	–	–	–	–	0.99	0.75
(E5)	0.91	1.11	0.53	1.14	0.97	0.98	0.69	0.87	1.12	0.95

(E4) and (E5) are the nonlinear difference reconstructions with and without ROI constraint.

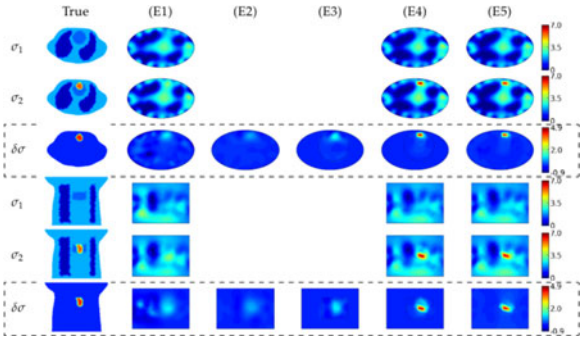

Fig. 6. Case 2: Horizontal and vertical cross sections at the level of $z = 20$ cm and $y = 10$ cm, respectively. The true conductivity (top row) and the estimates (E1)–(E5) described in Section IV-C. The dashed boxes highlight the true and estimated conductivity change $\delta\sigma$. (E4) and (E5) are the nonlinear difference reconstructions with and without ROI constraint, respectively.

overestimates the contrast of $\delta\sigma$ quite heavily, RCo being 1.31. The estimate (E3) is more affected by the modeling errors than (E2). This behavior can be explained by the fact that in the ROI constrained linear approach, the effects of modeling errors which do not cancel out in the subtraction $V_2 - V_1$, are propagated into a smaller dimensional subspace than in the whole domain estimate (E2), leading to heavy artifacts in the ROI.

The estimates (E4) and (E5) based on nonlinear difference imaging lead to the most accurate reconstructions of the conductivity change $\delta\sigma$—RCR and RCo being, respectively, 0.86 and 1.12 for the estimate (E4), and 0.9 and 1.11 for (E5). It is worth noticing that in (E4) and (E5), the reconstructed conductivity change $\delta\sigma$ is feasible *although* the reconstructed conductivity distributions σ_1 and σ_2 are heavily biased (see Fig. 5). As pointed out in [20], this results from the parametrization used in (E4) and (E5): When modeling errors remain unchanged between observations V_1 and V_2, the errors caused by the mismodeling are absorbed by the estimate of σ_1, which consists of the parameters that are common for the models of both V_1 and V_2.

B. Case 2: Cardiac Imaging With EIT

The results of Case 2 are shown in Fig. 6. The conductivity change can be detected in all the estimates (E1)–(E5), and

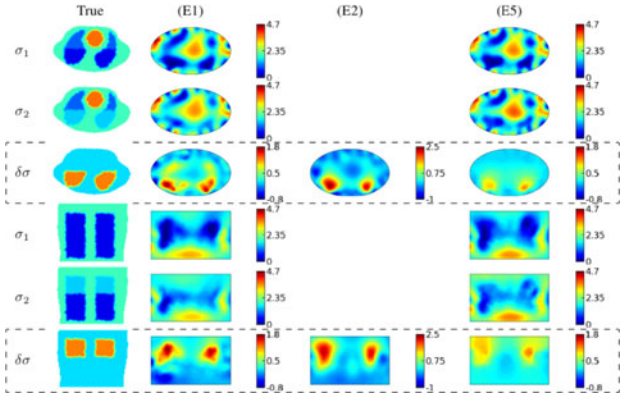

Fig. 7. Case 3: Lung imaging without a shape change of the thorax. Horizontal and vertical cross sections at the level of $z = 22.5$ cm and $y = -8.5$ cm, respectively. The true conductivity (top row) and the estimates (E1), (E2), and (E5) described in Section IV-C. The dashed boxes highlight the true and estimated conductivity change $\delta\sigma$. (E5) is the nonlinear difference reconstructions without ROI constraint.

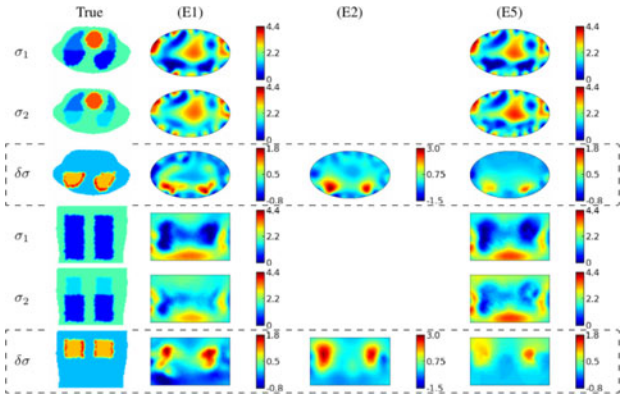

Fig. 8. Case 4: Lung imaging with a change of the thorax shape, otherwise as in Fig. 7.

qualitatively all the estimates of the conductivity change are free of significant reconstruction artifacts. Estimates (E1)–(E3) overestimate the size of the change $\delta\sigma$, and in the estimates (E4) and (E5), the size is underestimated. However, the quantitative contrast is again clearly the best in the nonlinear estimates (E4) and (E5), see Table IV.

C. Cases 3 and 4: Lung Imaging With EIT

In the lung imaging (Cases 3 and 4), we only considered the whole domain estimates (E1), (E2), and (E5), since the ROI would cover a significant part the overall volume of the chest, and in the Case 4, where the chest deformation between the states is included in the simulation, the selection of the ROI would be somewhat ambiguous.

Fig. 7 shows the results of Case 3 where the shape of the chest does not change between the states. The conductivity change can be detected in all the estimates (E1), (E2), and (E5). However, the CRs and the RCo are clearly the best in the estimate (E5), see Table IV.

The results of Case 4 are shown in Fig. 8. As expected, the reconstructed conductivity changes in all the estimates are worse compared to Case 3, due to the change of the chest shape

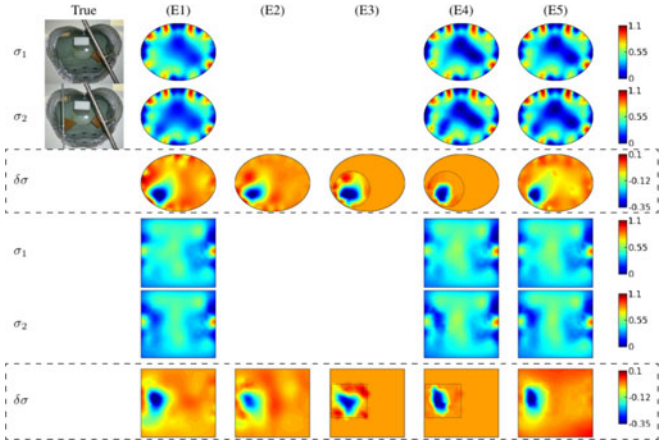

Fig. 9. Case 5: The measurement phantom and the reconstructions obtained by estimates (E1)–(E5) described in Section IV-C with real data. (E4) and (E5) are the nonlinear difference reconstructions with and without ROI constraint, respectively.

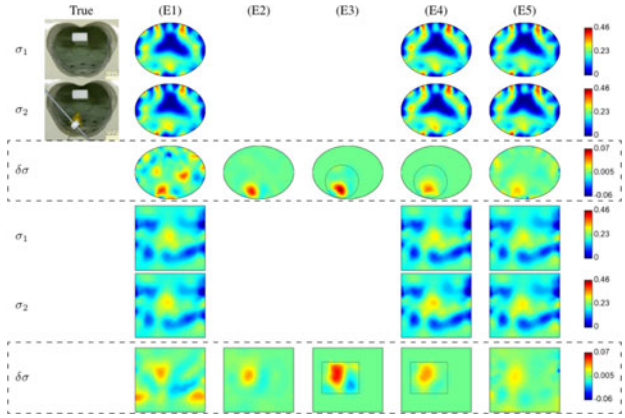

Fig. 10. Case 6: The measurement phantom and the reconstructions obtained by estimates (E1)–(E5) described in Section IV-C with real data. (E4) and (E5) are the nonlinear difference reconstructions with and without ROI constraint, respectively.

between the measurements V_1 and V_2. However, the performance of the approaches compared to each other remains similar to the more ideal case 3; the estimate (E5) gives again quantitatively the most accurate reconstruction of the conductivity change.

In overall, the results of the simulated test cases indicate that the nonlinear approach improves the accuracy of the estimates of $\delta\sigma$ compared to the linear approach, and that the approach tolerates inexact knowledge of the body shape at least to the same extent as the linear approach. The result of Case 4 indicates that this also extends to the cases where the modeling errors are not invariant between the states.

D. Reconstructions Using Experimental Data

In the reconstructions, an elliptic cylinder with height 30 cm, semimajor axis 21 cm, and semiminor axis 16 cm was used as the geometry in inverse computations. The initial guesses of $\sigma_{\mathrm{glob}} \in \mathbb{R}$ and $z_{\mathrm{glob}} \in \mathbb{R}$ for the water conductivity and contact impedances were computed by solving

$$[\sigma_{\mathrm{glob}}, z_{\mathrm{glob}}]^{\mathrm{T}} = \arg\min_{\sigma, z>0} \|L_e(V_1 - U(\sigma, z))\|^2.$$

In both experimental cases (Cases 5 and 6,), the estimated water conductivity was $\sigma_{\mathrm{glob}} = 0.18\,\mathrm{mS}\cdot\mathrm{cm}^{-1}$. The estimated contact impedance was $z_{\mathrm{glob}} = 550\,\Omega\cdot\mathrm{cm}^2$ in Case 5, and $z_{\mathrm{glob}} = 443\,\Omega\cdot\mathrm{cm}^2$ in Case 6.

Figs. 9 and 10, respectively, show the results of Case 5 and Case 6 described in Section IV-F. The CRs of the estimates are tabulated in Table IV. Contrast estimates were not available for the real data, since exact values for the conductivities of the plastic objects and rutabaga were not known.

In Case 5 (see Fig. 9), the conductivity change was detected in all the estimates (E1)–(E5), despite the significant error in the shape of the domain model. Based on a visual assessment, estimate (E4) leads to the best reconstruction of $\delta\sigma$—the shape of the resistive inclusion is detected relatively well and the reconstruction of $\delta\sigma$ is free from major artifacts. Estimate (E4) also results in the CR closest to the true value, RCR being 0.99, see Table IV.

Also, in Case 6 (see Fig. 10), all estimates (E1)–(E5), are able to detect the conductivity change $\delta\sigma$ in the location of the rutabaga, although the contrast of the inclusion with respect to the background is much smaller than in Case 5. The reconstructions show that the conductivity of the rutabaga is slightly higher than the background conductivity, thus resulting in a positive change of the conductivity. Based on a visual assessment, (E2) and (E4) give the best reconstruction of $\delta\sigma$. Further, estimate (E4) leads to a CR closest to the true value, RCR being 0.75, see Table IV.

VI. Conclusion

In this paper, we applied the recently proposed nonlinear difference imaging approach to 3-D EIT in the presence of geometrical modeling errors. In the nonlinear approach, the conductivity after the change is represented as a linear combination of the (unknown) initial conductivity and the conductivity change, and the EIT inverse problem is formulated as simultaneous reconstruction of the initial conductivity and the change based on the EIT datasets collected before and after the change. The approach allows the use of different spatial models for the initial conductivity and the change by different regularization functionals, and also the use of a ROI constraint for the conductivity change.

The feasibility of the nonlinear approach was evaluated in geometries related to three potential medical applications of EIT: glottal, cardiac, and lung imaging. The performance of the nonlinear approach was studied by simulations and experimental data from a laboratory setup. The results were compared against the reconstructions of the conductivity change with separate absolute reconstructions and conventional linear reconstruction. The results demonstrate that the nonlinear difference reconstructions tolerate significant geometrical modeling errors at the least to same extent as the conventional linear approach and produce quantitatively more accurate reconstruction of the conductivity change. The result of this paper suggests that the

nonlinear approach could be used to improve the accuracy and specificity of EIT in the medical applications.

ACKNOWLEDGMENT

The authors would like to thank Prof. R. G. Lima from the University of Sao Paulo, Brazil, for sharing his CT dataset of larynx, and Dr. E. León and Dr. F. Moura for their help with 3-D mesh generator.

REFERENCES

[1] I. Frerichs, "Electrical impedance tomography (EIT) in applications related to lung and ventilation: A review of experimental and clinical activities," *Physiol. Meas.*, vol. 21, no. 2, pp. R1–R21, 2000.

[2] I. Frerichs *et al.*, "Detection of local lung air content by electrical impedance tomography compared with electron beam CT," *J. Appl. Physiol.*, vol. 93, no. 2, pp. 660–666, 2002.

[3] V. Cherepenin *et al.*, "Three-dimensional EIT imaging of breast tissues: System design and clinical testing," *IEEE Trans. Med. Imag.*, vol. 21, no. 6, pp. 662–667, Jun. 2002.

[4] Y. Zou and Z. Guo, "A review of electrical impedance techniques for breast cancer detection," *Med. Eng. Phys.*, vol. 25, no. 2, pp. 79–90, 2003.

[5] G. Boverman *et al.*, "Robust linearized image reconstruction for multifrequency EIT of the breast," *IEEE Trans. Med. Imag.*, vol. 27, no. 10, pp. 1439–1448, Oct. 2008.

[6] P. Vauhkonen *et al.*, "Three-dimensional electrical impedance tomography based on the complete electrode model," *IEEE Trans. Biomed. Eng*, vol. 46, no. 9, pp. 1150–1160, Sep. 1999.

[7] D. Barber and B. Brown, "Applied potential tomography," *J. Phys. E, Sci. Instrum.*, vol. 17, no. 9, pp. 723–733, 1984.

[8] D. Barber and A. Seagar, "Fast reconstruction of resistance images," *Clin. Phys. Physiol. Meas.*, vol. 8, no. 4A, pp. 47–54, 1987.

[9] B. Brown, "Electrical impedance tomography (EIT): A review," *J. Med. Eng. Technol.*, vol. 27, pp. 97–108, 2003.

[10] A. P. Bagshaw *et al.*, "Electrical impedance tomography of human brain function using reconstruction algorithms based on the finite element method," *Neuroimage*, vol. 20, no. 2, pp. 752–764, 2003.

[11] A. Adler *et al.*, "Impedance imaging of lung ventilation: Do we need to account for chest expansion?" *IEEE Trans. Biomed. Eng.*, vol. 43, no. 4, pp. 414–420, Apr. 1996.

[12] V. Kolehmainen *et al.*, "Assessment of errors in static electrical impedance tomography with adjacent and trigonometric current patterns," *Physiol. Meas.*, vol. 18, no. 4, pp. 289–303, 1997.

[13] M. Soleimani *et al.*, "Imaging of conductivity changes and electrode movement in EIT," *Physiol. Meas.*, vol. 27, no. 5, pp. S103–S113, 2006.

[14] A. Boyle and A. Adler, "The impact of electrode area, contact impedance and boundary shape on EIT images," *Physiol. Meas.*, vol. 32, no. 7, pp. 745–754, 2011.

[15] A. Boyle *et al.*, "Shape deformation in two-dimensional electrical impedance tomography," *IEEE Trans. Med. Imag.*, vol. 31, no. 12, pp. 2185–2193, Dec. 2012.

[16] D. Holder and A. Khan, "Use of polyacrylamide gels in a saline-filled tank to determine the linearity of the sheffield mark 1 electrical impedance tomography (EIT) system in measuring impedance disturbances," *Physiol. Meas.*, vol. 15, no. 2A, pp. A45–A50, 1994.

[17] G. Hahn *et al.*, "Imaging pathologic pulmonary air and fluid accumulation by functional and absolute EIT," *Physiol. Meas.*, vol. 27, no. 5, pp. S187–S198, 2006.

[18] T. N. Tallman *et al.*, "Damage detection and conductivity evolution in carbon nanofiber epoxy via electrical impedance tomography," *Smart Mater. Struct.*, vol. 23, no. 4, p. 045034, 2014.

[19] D. Liu *et al.*, "Estimation of conductivity changes in a region of interest with electrical impedance tomography," *Inverse Problems Imag.*, vol. 9, no. 1, pp. 211–229, 2015.

[20] D. Liu *et al.*, "A nonlinear approach to difference imaging in EIT; Assessment of the robustness in the presence of modelling errors," *Inverse Problems*, vol. 31, no. 3, p. 035012, 2015.

[21] M. Kob and T. Frauenrath, "A system for parallel measurement of glottis opening and larynx position," *Biomed. Signal Process. Control*, vol. 4, pp. 221–228, 2009.

[22] D. Isaacson *et al.*, "Imaging cardiac activity by the D-bar method for electrical impedance tomography," *Physiol. Meas.*, vol. 27, pp. S43–S50, 2006.

[23] S. Zlochiver *et al.*, "Parametric EIT for monitoring cardiac stroke volume," *Physiol. Meas.*, vol. 27, no. 5, pp. S139–S146, 2006.

[24] K. S. Cheng *et al.*, "Electrode models for electric current computed tomography," *IEEE Trans. Biomed. Eng.*, vol. 36, no. 9, pp. 918–924, Sep. 1989.

[25] E. Somersalo *et al.*, "Existence and uniqueness for electrode models for electric current computed tomography," *SIAM J. Appl. Math.*, vol. 52, no. 4, pp. 1023–1040, 1992.

[26] L. M. Heikkinen *et al.*, "Simultaneous reconstruction of electrode contact impedances and internal electrical properties: II. Laboratory experiments," *Meas. Sci. Technol.*, vol. 13, no. 12, pp. 1855–1861, 2002.

[27] J. Mueller and S. Siltanen, *Linear and Nonlinear Inverse Problems With Practical Applications*. Philadelphia, PA, USA: SIAM, 2012.

[28] C. Gabriel *et al.*, "Electrical conductivity of tissue at frequencies below 1 mhz," *Phys. Med. Biol.*, vol. 54, no. 16, pp. 4863–4878, 2009.

[29] C. Lieberman *et al.*, "Parameter and state model reduction for large-scale statistical inverse problems," *SIAM J. Sci. Comput.*, vol. 32, pp. 2523–2542, 2010.

[30] L. I. Rudin *et al.*, "Nonlinear total variation based noise removal algorithms," *Physica D, Nonlinear Phenomena*, vol. 60, no. 1, pp. 259–268, 1992.

[31] A. Lipponen *et al.*, "Electrical impedance tomography imaging with reduced-order model based on proper orthogonal decomposition," *J. Electron. Imag.*, vol. 22, no. 2, p. 023 008, 2013.

[32] J. Bardsley *et al.*, "Randomize-then-optimize for sampling and uncertainty quantification in electrical impedance tomography," *SIAM J. Uncertainty Quantification*, vol. 3, pp. 1136–1158, 2015.

[33] G. Gonzalez *et al.*, "Experimental evaluation of 3D electrical impedance tomography with total variation prior," *Inverse Problems Sci. Eng.*, 2015, to be published (http://dx.doi.org/10.1080/17415977.2015.1113961).

[34] A. Detroyer and S. H. Loring, "Respiratory muscle action," in *Handbook of Physiology*, vol. 3. Betesda, MD, USA: Amer. Physiological Soc., 1985, ch. 26, sec. 3.

[35] W. F. Ganong and K. E. Barrett, *Review of Medical Physiology*, vol. 21. New York, NY, USA: McGraw-Hill, 2005.

[36] J. Kourunen *et al.*, "Suitability of a pxi platform for an electrical impedance tomography system," *Meas. Sci. Technol.*, vol. 20, no. 1, p. 015503, 2009.

[37] Y. Wan *et al.*, "Sensitivity study of an ultrasound coupled transrectal electrical impedance tomography system for prostate imaging," *Physiol. Meas.*, vol. 31, no. 8, pp. S17–S29, 2010.

[38] H. Dehghani *et al.*, "Excitation patterns in three-dimensional electrical impedance tomography," *Physiol. Meas.*, vol. 26, no. 2, pp. S185–S197, 2005.

Authors' photographs and biographies not available at the time of publication.